Granular Matter (2021) 23:94
https://doi.org/10.1007/s10035-021-01164-9

ORIGINAL PAPER

Investigating the effectiveness of Rolling Dynamic Compaction (RDC) using Discrete Element Method (DEM)

Yue Chen[1] · Mark B. Jaksa[1] · Yien-Lik Kuo[1] · David W. Airey[2]

Received: 7 October 2020 / Accepted: 31 August 2021 / Published online: 22 September 2021
© The Author(s), under exclusive licence to Springer-Verlag GmbH Germany, part of Springer Nature 2021

Abstract
Rolling dynamic compaction is a soil compaction technique which involves compacting the ground with a heavy, non-circular module. Compared with traditional compaction methods, it is, in most cases, more efficient, as it improves the soil to a greater depth and it facilitates more rapid ground improvement due to its higher travel speeds. However, to date, there is a limited understanding of the nature of the subsurface improvement as a result of RDC. This paper presents a three-dimensional finite element method (FEM)-discrete element method (DEM) model which simulates the movement of soil particles, and the porosity, and hence density, variations during the RDC process. The FEM-DEM model is developed using experimental tests, and the numerical results are in good agreement with the laboratory test results. The effectiveness of 1:13 scale models of the 4-sided, 8- and 12-tonne, Broons BH-1300 and BH-1300 HD impact rollers are analysed based on the soil porosity variations. The relationships between porosity, soil displacements and the motion of the roller module are also investigated. The results of this study demonstrate the capability of the FEM-DEM model to simulate reliably the ground improvement induced by RDC.

Keywords Rolling dynamic compaction · Impact roller · Ground improvement · Discrete element method

1 Introduction

Soil compaction is a common approach to improve the ground for engineering purposes. After compaction, the density and bearing capacity of the soil increase, which means that the ground has improved strength and stiffness resulting in reduced settlements and enhanced performance. Compaction of the ground facilitates the construction of structures on sites which would otherwise be considered less than ideal for such purposes. In the field, soil compaction is often achieved through the use of mechanical equipment, such as heavy tamping, drum and sheepsfoot rollers, and vibrating plates. The variety of soil compaction methods are generally divided into two sub-categories, static and dynamic, based on the type of applied compactive effort. Static compaction compresses the soil by the self-weight of the equipment, whereas dynamic compaction makes use of high energy impact forces in addition to the self-weight of the equipment. Rolling dynamic compaction (RDC) is a relatively new dynamic compaction method which has become increasingly popular in recent years. It involves towing a heavy (6–12 tonnes), non-circular (3-, 4- and 5-sided) module behind a tractor to achieve soil compaction. The module rotates about its corner and falls to impact the ground. Mechanical energy induced by the roller increases the soil density by rearranging the soil particles and reducing the voids within the soil. Compared with conventional static and vibratory compaction techniques, RDC improves the ground to a greater depth, typically between 1–3 m, depending on soil type and ground conditions [1]. In addition, RDC is effective when it is applied to large and open sites, since it can travel at a speed of 10–12 km/h, whilst traditional drum rollers travel at 4 km/h [2]. Field tests have

✉ Yue Chen
yue.chen@adelaide.edu.au

Mark B. Jaksa
mark.jaksa@adelaide.edu.au

Yien-Lik Kuo
yien.kuo@adelaide.edu.au

David W. Airey
david.airey@sydney.edu.au

[1] School of Civil, Environmental and Mining Engineering, University of Adelaide, Adelaide, SA 5005, Australia

[2] School of Civil Engineering, University of Sydney, Sydney, NSW 2006, Australia

been undertaken by previous researchers [1, 3–5] to assess the efficacy of RDC. Several in situ tests were conducted to measure the energy transfer, the zone of influence and the ground settlement induced by RDC. Since undertaking field tests is expensive and time consuming, Rajarathnam et al. [6] studied the effectiveness of RDC using a 1:20 physical scale model of a 3-sided module and Chung et al. [7] and Chen et al. [8] employed a 1:13, 4-sided scale model. The use of small scale models allows RDC to be assessed in a controlled laboratory environment and avoids conducting expensive field tests. According to Chung et al. [7], the 1:13 physical scale model produces similar ground responses to the full-size prototype based on the scaling law developed by Altaee and Fellenius [9]. Chen et al. [8] evaluated the effectiveness of the physical scale model from four aspects, namely ground settlement, improvement depth, the optimum number of rolling passes, and the optimal operating speed. Although conducting small-scale tests is more efficient than carrying out field trials, small-scale tests still require time and effort to prepare and undertake the tests, and the relationship between the laboratory and field measurements is a topic for ongoing research. With the development of high performance computers, numerical simulations have been adopted by many researchers to study ground responses induced by RDC. The finite element method (FEM) was adopted by Kuo et al. [10] and Bradley et al. [11] to simulate the behaviour of a full-size, 4-sided RDC module using the LS-DYNA [12] computer program. Soil settlements and influence stresses obtained from the FEM model were validated using field test results for both static and dynamic loadings. The FEM model was shown to be capable of predicting soil displacements and soil stresses under the impact roller. In addition, the FEM model was used to estimate the energy imparted to the soil by RDC [11]. Although, the FEM model has shown encouraging results in terms of simulating the ground response induced by RDC, the motion of soil particles and porosity (and hence density) changes within soil mass remain elusive, given the limitations of constitutive models and continuum based methods, such as FEM, more generally.

The discrete element method (DEM) was introduced by Cundall and Strack [13] to simulate the behaviour of granular materials. Given that soils are particulate materials, DEM provides a better understanding of the micromechanical behaviour of soil at the particle scale. Soil particles are modelled in DEM as undeformable spheres with deformable contacts [14]. One of the advantages of DEM is that it can track the movement of every individual particle to provide detailed information about the deformation of the entire soil body, which offers opportunities to simulate soil particles under large deformations.

Since the traditional FEM is used routinely in geotechnical engineering to simulate the deformation of a soil mass, but it is unable to model the micromechanical behaviour of particles, and DEM is able to model particle movements and interactions, there is a need to combine the advantages of these two methods into a single numerical model in order to increase the efficacy of the numerical simulation. A FEM-DEM combined approach has been applied to simulate the dynamic packing and quasi-static interactions of granular particles [15] and to assess wear of a tipper using LS-DYNA [16]. These studies demonstrated the capabilities and accuracy of the combined FEM-DEM approach when simulating geomechanical problems.

This paper develops a three-dimensional FEM-DEM model to simulate granular particles and the results of this model are then used to analyse the behaviour of 1:13 scale models of the 4-sided, 8- and 12- tonne, Broons BH-1300 and BH-1300 HD impact rollers, respectively. In the numerical simulation, soil particles are modelled using the DEM and the 4-sided scaled module is simulated by the FEM, which is similar to the numerical, full-size RDC model developed by Kuo et al. [10] and Bradley et al. [11], but with scaled properties. The numerical model is validated against experimental results obtained by Chen et al. [8], as discussed below.

2 DEM modelling

2.1 Basic features

The commercial software LS-DYNA is used to perform the FEM-DEM simulation in this study. Since particle movements and interactions are the main focuses of this study, a three-dimensional numerical simulation is applied to model better the behaviour of soil particles. In DEM, granular materials are simplified as rigid spheres with soft contacts, which means particles are permitted to overlap at contact points. The macroscopic behaviour of granular materials is captured by interactions between particles. In general, DEM consists of two main stages. The first stage is using a contact model to describe the forces acting on the particles. Subsequently, Newton's second law of motion is adopted to calculate particle displacements at each time step based on any unbalanced forces. There are a number of contact models to simulate interactions between particles, that vary from linear to the highly non-linear. The linear contact model is the most popular and widely used since it is simple and efficient. It has fewer parameters that need to be calibrated when compared with other contact models. Complex highly non-linear contact models require more computational time to run the model and to calibrate the microscopic parameters. Previous research has shown that the linear contact model is able to appropriately replicate the properties of granular materials and it can be used reliably to study geotechnical

problems [14, 17–19]. As a result, the linear contact model is adopted in this study. In this model, the contact forces between two overlapped particles are represented by a linear spring and a dashpot in the normal direction, a linear spring and a dashpot in the shear direction, and a frictional slip is permitted in the shear direction with a coefficient of friction. Therefore, in total, five microscopic parameters are needed as inputs, namely the normal and shear stiffnesses (k_n and k_s, respectively), normal and shear damping ratios (β_n and β_s, respectively), and the coefficient of friction (μ). These input parameters can be determined through a calibration approach, which is often achieved using standard geotechnical tests, such as the direct shear, biaxial/triaxial or uniaxial compression tests [20]. Similar to the interaction between finite elements, the contact between discrete particles and finite elements is defined using a penalty-based contact algorithm, if penetration of the discrete particles, through the contact surface of the finite elements, is identified [12]. The contact force is proportional to the penetration depth, which is treated by placing springs between the contact elements. The stiffnesses of these springs define the magnitude of the contact forces, which are calculated using Eq. (1). If the stiffnesses of the contact elements are different, LS-DYNA adopts the minimum stiffness. The contact frictional force is calculated based on Coulomb's law of friction, if there is sliding between the contacts.

$$k_i = \frac{f_s \bullet A_i \bullet K_i}{V_i} \tag{1}$$

where k_i is the stiffness of the spring (i) placed between particles and the contact finite elements; f_s is the penalty scale factor (the default value of unity is used in the simulations); and A_i, V_i and K_i are the contact area, the volume and the stiffness of the contacted elements, respectively.

As mentioned above, experimental 1:13 scale model tests were conducted by Chen et al. [8], and the results of these tests are used to validate the FEM-DEM model in this study. The experimental scale model tests involved using a 1:13 scale 4-sided RDC module to traverse an acrylic chamber (300 mm long × 280 mm wide × 250 mm high) which was filled with fused quartz. Internal displacements of the soil particles along the centreline of the module traverse lane were captured using a conventional charge-coupled device (CCD) camera, and the soil displacement fields were obtained using the *GeoPIV_RG* MATLAB module, which is an implementation of the particle image velocimetry (PIV) technique. In this study, LS-DYNA is used to simulate the experimental process adopted by Chen et al. [8]. The behaviour of the fused quartz is simulated by the DEM. Since fused quartz particles are angular in shape, in order to mimic the irregular shape of fused quartz without introducing any new microscopic parameters that need to be calibrated, the rotation of the spheres in the DEM model is restricted. This method is efficient as it increases the macroscopic shear strength of the numerical models without changing the shape of particles or introducing additional input parameters. According to Calvetti et al. [21], Calvetti et al. [22] and Gabrieli et al. [14], the rotation of particles was prohibited to constrain the effects of the spherical shape, since spheres perform rotational movements relatively easily. They reported that the capability of numerical models to replicate the behaviour of granular materials was unaffected by prohibiting the rotation of spheres, if the microscopic friction coefficient was calibrated accordingly.

According to Wang and Leung [23], quartzose material has a bulk modulus to shear modulus ratio close to 1. Therefore, in the numerical simulations that follow, the ratio between the normal and shear stiffnesses is chosen to be 1. As shown in Eq. (2), the damping ratio (β) of the dashpots between the DEM particles relates to the coefficient of restitution (COR) [24], which is defined as the ratio of the velocities after and before impact between the particles. The COR for contact between quartzose material is approximately 0.8 from drop test results [25], which then yields the damping ratio of approximately 0.07. In addition, a small numerical damping ratio ($\beta = 0.1$) was suggested by Gabrieli et al. [14] to better simulate the triggering of failure. Therefore, small numerical normal and shear damping ratios ($\beta_n = \beta_s = 0.1$) are selected in all simulations, considering the value of the COR and the simulation of the triggering of failure.

$$\beta = -\frac{\ln e}{\sqrt{(\ln e)^2 + \pi^2}} \tag{2}$$

where β is the damping ratio of viscous dashpots; and e is the coefficient of restitution.

2.2 DEM input parameters calibration

DEM input parameters were calibrated against consolidated drained (CD) triaxial tests performed by the authors on dry fused quartz with the same grading as used in the physical model experiments [8]. Figure 1 presents the experimental and numerical particle size distribution curves. The size of the experimental fused quartz is between 3 to 5 mm, with $D_{50} = 3.84$ mm (black solid line). The particle sizes adopted in the numerical simulations of the triaxial tests (black dashed line) were very similar to the experimental tests. In the numerical model, spherical particles were generated according to a Gaussian distribution by specifying the maximum and minimum diameters, and a mean of 4 mm.

Conventional triaxial tests were performed on samples, which were 50 mm in diameter and 100 mm high. Numerical simulations of these tests were performed using the configuration shown in Fig. 2. The finite elements were used to model

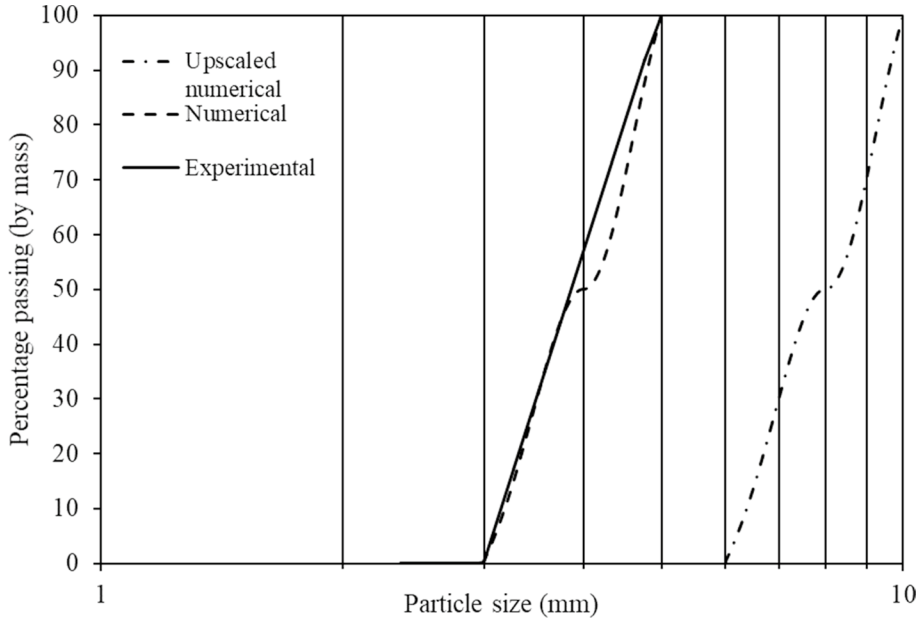

Fig. 1 Numerical and experimental particle size distribution curves

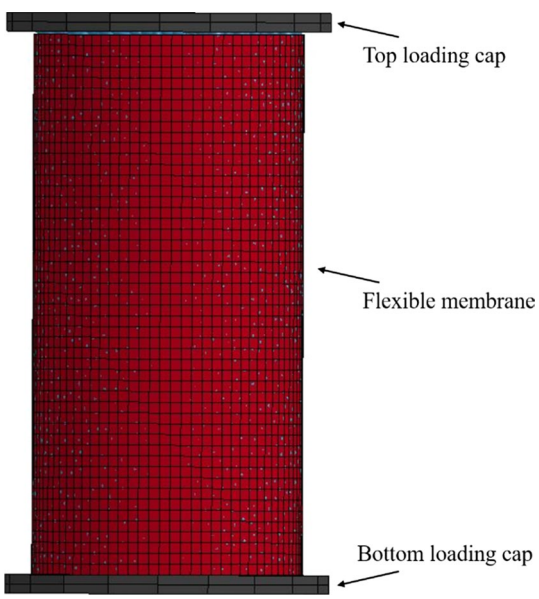

Fig. 2 Numerical triaxial test sample

the flexible membrane and two loading caps, while the DEM was employed to simulate soil particles. The friction coefficient between the DEM particles and the finite elements were obtained from a numerical inclined plane test, which has been used by several researchers [26, 27]. In the laboratory, fused quartz triaxial samples were prepared by dry pluviation into a mould. In the numerical simulations, spheres were generated randomly to fill an enclosed cylinder and then pluviated into the membrane under gravity at a relatively constant height. Particles were slightly filled above the level of the membrane to permit modest compaction. The top loading cap was then moved up and down by 20 mm at 200 mm/s for 2 s to compact the particles and to match the experimental porosity. A total of approximately 3,500 particles were used in the triaxial test simulations. When the particles reached an equilibrium state, the confining pressures were applied to the sample equally in all directions and were maintained during the tests. Three confining pressures were simulated in this study, 25, 50 and 100 kPa. During the shearing stage, axial strain was applied by displacing the top plate vertically at a constant velocity, which was slow enough to ensure a quasi-static condition, until the axial strain reached 20%. Axial strain was calculated from the displacement of the top loading cap, while stresses were determined from the contact forces between the top loading cap and the particles in contact with the top cap. In the physical triaxial tests, the loading rate was set at 1 mm/min. However, due to the computational and time constraints, the numerical samples were sheared at a higher loading rate. The effects of different loading rates on the numerical triaxial tests results were investigated, and a loading rate of 10 mm/s was chosen in all triaxial test simulations, as it is the fastest loading rate which provided a computationally efficient and reliable model. A similar procedure for selecting an appropriate loading rate for numerical triaxial tests was reported by Mahabadi et al. [28], Kozicki et al. [29] and Gu et al. [30]. In addition, as suggested by Da Cruz et al. [31], Xu et al. [32], Zhang et al. [33] and Wu et al. [34], the inertial number should smaller than 10^{-3} to maintain a quasi-static condition in the numerical model. Based on Eq. (3), the maximum inertial number was approximately $1.07 \times 10^{-4} < 10^{-3}$, which indicated the numerical triaxial tests were conducted in a quasi-static condition during the shearing stage. The minimum pressure along the top and bottom loading caps was approximately 902 kPa when the top loading cap was moved up and down to compact the particles; therefore,

the maximum inertial number was 3.57×10^{-4}, which implied the numerical particle assembly was in a quasi-static condition during sample preparation.

$$I = \dot{\varepsilon}\sqrt{\frac{m}{pd}} \tag{3}$$

where I is the inertia number; $\dot{\varepsilon}$ is the shear strain rate; m and d are the mass and diameter of particles, respectively; and p is the confining pressure.

The calibration process involved an iterative, trial-and-error approach, where the five numerical inputs were varied in-turn, until the numerical results conformed to the experimental measurements. The final calibrated result is shown in Fig. 3. As can be seen, in general, the experimental triaxial tests results are well predicted by the numerical

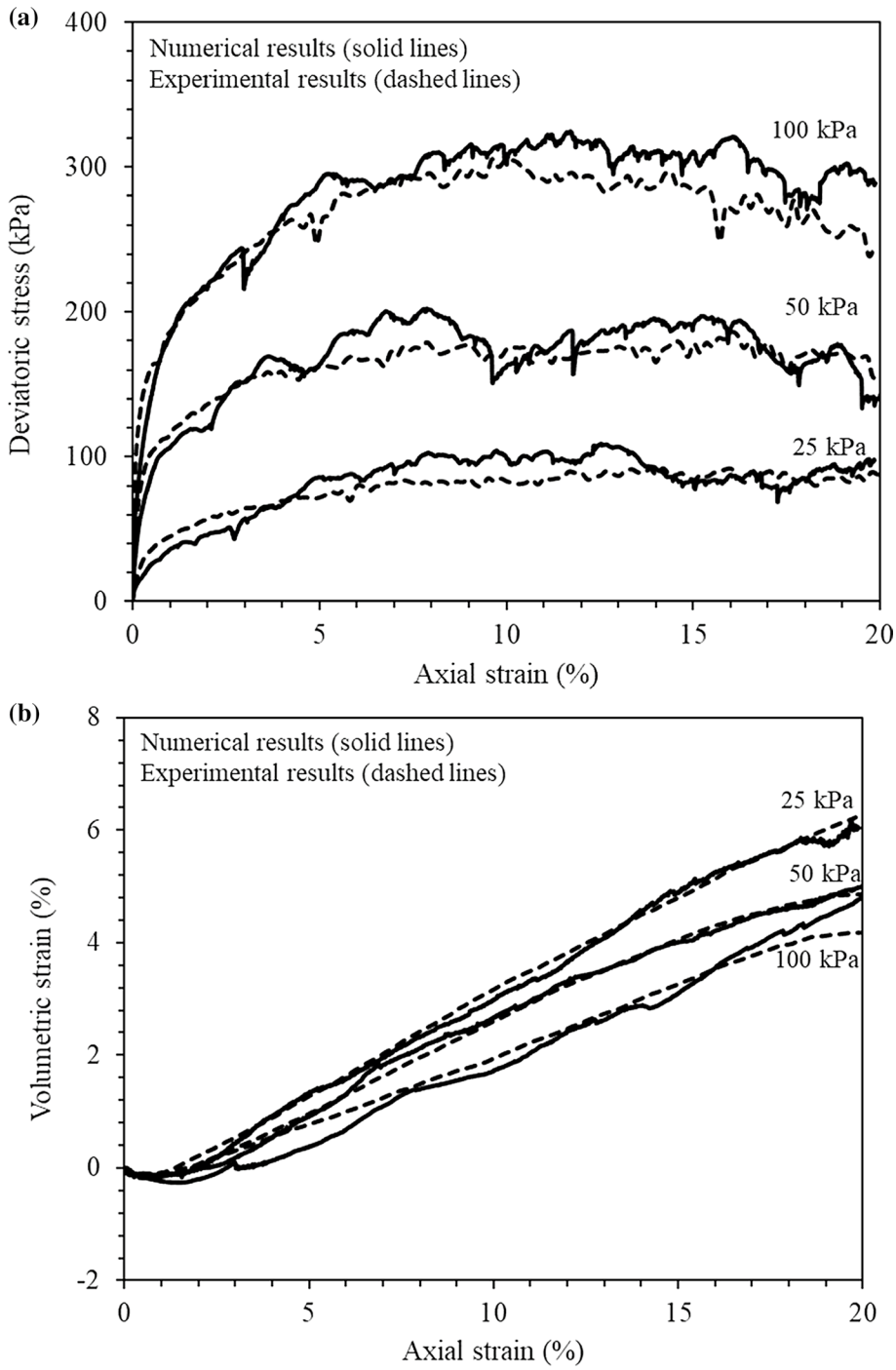

Fig. 3 Experimental and numerical triaxial test results at confining pressures of 25, 50 and 100 kPa: **a** stress–strain curves, **b** volumetric curves

model; although the peak deviatoric stresses are somewhat overestimated, and volumetric strains are slightly underestimated by the numerical model. As can also be observed, the numerical stress–strain results show a degree of fluctuation, and this is because the contact stiffness between particles is relatively high, which causes the numerical model to be less stable. The same phenomenon was reported by Sadek and Chen [35] and Nandanwar [36]. As the contact stiffness increases, greater fluctuation is shown in stress–strain curves, or in other words, a higher stiffness leads to a less stable model. Overall, the numerical stress–strain curves are in good agreement with the experimental results.

The obtained, calibrated DEM input parameters are shown in Table 1. Since the size of the numerical particles was randomly generated according to a Gaussian distribution, in order to assess the effects of the randomly generated particles on the simulation results, all numerical triaxial tests were performed three times for each confining pressure, and the numerical particles were generated randomly each time. The numerical stress–strain curves presented in Fig. 3 are the average of the three results obtained for each confining pressure.

3 Simulation of RDC

3.1 RDC model setup

In order to validate the behaviour of spherical particles using the calibrated DEM input parameters, the RDC simulation was conducted in the same manner as that of experimental tests (Fig. 4). Therefore, a numerical model was developed which consisted of a simplified impact roller module, a chamber filled with DEM particles and two timber frames, as shown. Similar to Fig. 4a, the roller travels from right to left and it compacts particles within the chamber in Fig. 4b. The chamber was set to the same dimensions as that used in the experimental tests, namely 300 mm length × 280 mm width × 250 mm height. The chamber and the two timber frames were modelled using the FEM, as rigid bodies with no deformation or displacement permitted. In the numerical RDC simulations, the DEM particles were generated in a process similar to that adopted in the numerical triaxial tests. Particles were generated randomly to fill an enclosed box and then pluviated in successive layers into the chamber under gravity from the same approximate height of 280 mm. After the particles reached equilibrium, a rigid plate was placed on top of the particles, and moved up and down by 15 mm at 150 mm/s for 1 s to compact each of the soil layers. The minimum pressure along the rigid plate and the bottom of the chamber was approximately 1,109 kPa when the rigid plate compacted the soil. According to Eq. (3), the maximum inertial number was 9.67×10^{-4}, which indicated that the RDC model was in a quasi-static condition during the sample preparation stage. The assemblage porosity adopted in the numerical RDC simulations was 0.426, which accords with that used in the experiments (0.421). The numerical roller module used in this study was similar in shape to the full-size model used by Kuo et al. [10] and Bradley et al. [11], but to be consistent with the experiments a 1:13 scaled model was replicated, which is also shown in Fig. 4a. As described by Kuo et al. [10] and Bradley et al. [11], the roller is effectively rigid relative to the stiffness of the soil and hence, the deformation of the roller during compaction is negligible. Therefore, in the numerical model, the roller was simulated using finite elements and defined as a rigid material. The adoption of the FEM is necessary to simulate the boundaries and the roller. The timber frames, at each end of the chamber, were modelled using the FEM to facilitate the compaction process. In addition, it is important to accurately simulate the complex characteristics of the roller module, since these significantly affect the ground improvement results [37]. The FEM is able to simulate the roller module accurately and efficiently. The numerical roller module was developed based on a computer aided drawing (CAD) that was provided by Broons, which is an accurate representation of the Broons' impact roller. The Young's modulus of elasticity and Poisson's ratio of the roller were 210 GPa and 0.28, respectively. The properties (such as, dimensions, weights and operating speeds) of the 1:13 impact roller modules were converted from the full-size prototypes using the scaling laws [Eqs. (4) to (6)] suggested by Altaee and Fellenius [9]. In this study, the geometric scale ratio (n) is 1/13. Two different weights of modules (3.64 and 5.46 kg) were studied, with identical dimensions of 115 × 115 × 100 mm (height × length × width), which correspond to the 8- and 12-tonne impact rollers (Broons BH-1300 and BH-1300 HD), respectively.

$$\frac{V_m}{V_p} = n \tag{4}$$

$$\frac{L_m}{L_p} = n \tag{5}$$

Table 1 Microscopic parameters used in DEM simulations

Parameter	Value
Specific gravity	2.20
Particle diameter (mm)	3–5
Coefficient of friction	0.306
Normal and shear stiffnesses (k_n and k_s) (N/m)	9.3×10^5
Normal and shear damping ratios (β_n and β_s)	0.1

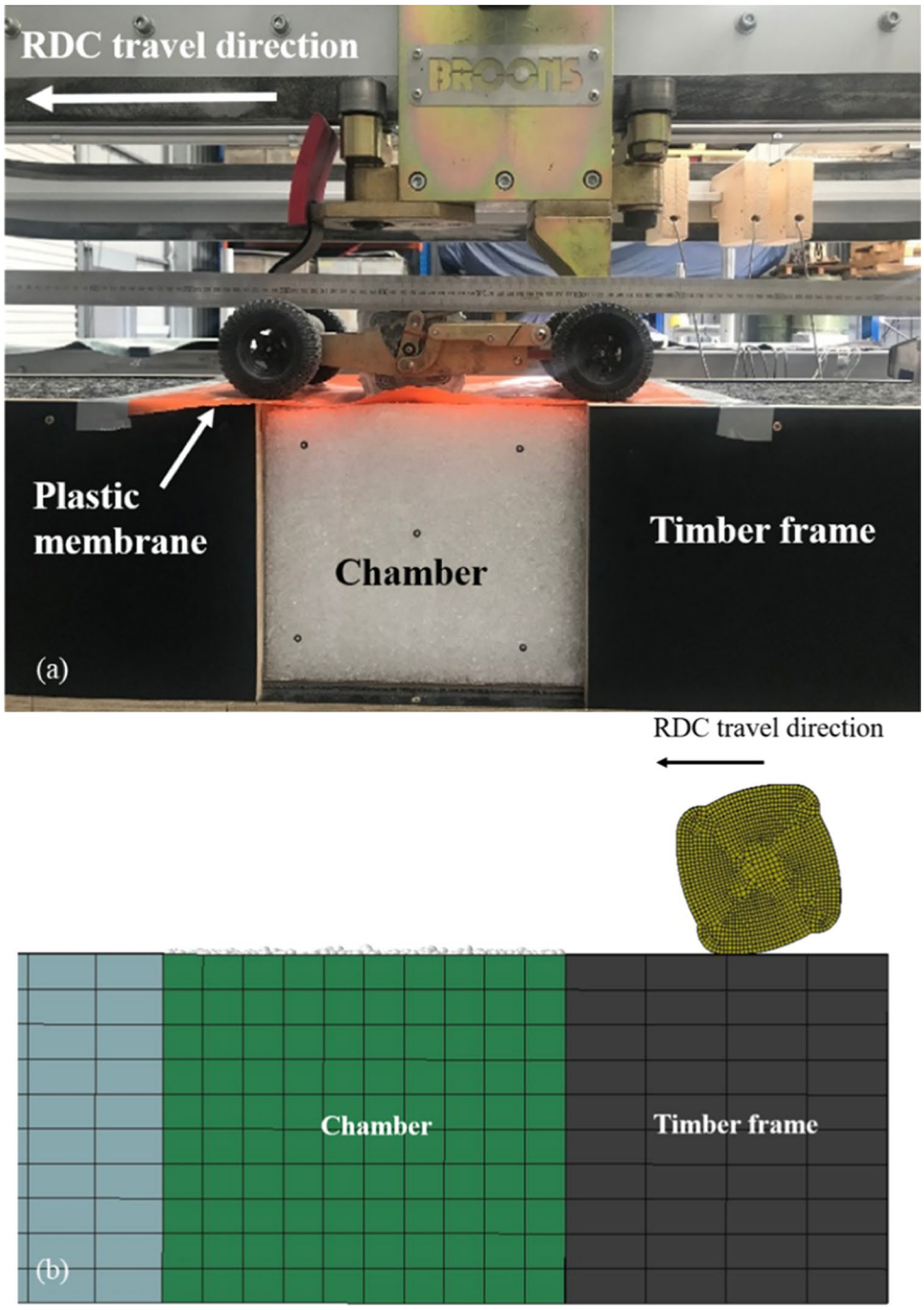

Fig. 4 Setup of RDC tests: **a** experimental setup, **b** numerical setup

$$\frac{M_m}{M_p} = n^3 \tag{6}$$

where V represents the operating speed; L is the characteristic length; M is the mass; n is the geometric scale ratio; and the subscripts m and p denote the scale model and prototype, respectively.

Particle sizes used in the numerical calibration tests were the same as the fused quartz sizes used in the experiments. Since the dimensions of triaxial tests samples were relatively small this resulted in a manageable number of numerical particles. However, in order to compare the numerical simulation results with the measurements from the experimental tests, the dimensions of the chamber used in the simulations needs to be the same. If actual particle sizes are used in the numerical simulation, a large number of particles (approximately 400,000) will be required, which is computationally intensive and time-consuming. Therefore, to obtain an appropriate balance between the computational time and the numerical accuracy, the particles were all scaled up to be

two times larger than the actual particle sizes. Diameters of the scaled particles were 6–10 mm, which consequently reduced the number of particles to approximately 42,000. The scaled particle size distribution is included in Fig. 1, shown previously. Since all the particles were scaled up, the shape of the particle size distribution curve remained the same and, as shown by Yang et al. [38], the porosity of the samples is independent of the particle scaling factor. The porosity of the particles near the boundaries of the chamber may be altered. However, similar to Chen et al. [8], to minimise boundary effects, ground improvement is investigated solely in the central region of the module traverse lane. In addition, as reported by Chen et al. [8], the most significant ground improvement occurred within the upper 150 mm depth and displacements of soil particles near the bottom of the chamber are negligible after 40 module passes. Therefore, ground improvement near the bottom of the chamber is insignificant. The upper limit of particle scaling is related to the dimensions of the model. In this study, the dimensions of the roller module is relevant, which affects the loaded surface that is directly in contact with the particles. Since the width (100 mm) is smaller than the length (115 mm) of the module, the width is the most relevant dimension and it determines the upper limit of particle scaling. The D_{50} of the scaled particles (8 mm) is one order of magnitude less than the width of the module (100 mm), which ensures an adequate number of particles remain in the model. This is consistent with Ciantia et al. [39], who reported that the dimension of model was always one order of magnitude above the scaled average particle diameter, to ensure that the macroscopic responses of the particles were maintained after scaling. This same issue was addressed by Tatsuoka [40] who stated that the dimensions of the model needed to be at least ten times more than the average scaled particle sizes to avoid size effects.

Since the particles have been scaled up, the calibrated DEM input parameters also need to be scaled to ensure that the geometrical properties of the particles remain constant [14]. A mass scaling (particle density remains constant before and after scaling) is applied in this study. This scaling law has been adopted in many studies, such as Gabrieli et al. [14], Evans and Valdes [41], Ciantia et al. [42], Zhou et al. [43] and Wang et al. [44]. According to the mass scaling law, Young's modulus, the ratio between the shear and normal stiffnesses, the friction coefficient and damping ratios are scale invariant. The normal stiffness depends on the particle scaling factor and has a linear relationship with respect to particle diameter [14, 45]. Hence, the value of normal stiffness is scaled up by a factor of 2 to equal 1.86×10^6 N/m. Table 2 presents the scaled DEM input parameters that are used in the RDC simulations that follow.

In LS-DYNA, the equations of motion are solved using the explicit central difference scheme. Therefore, the stability of the numerical model is conditioned to the employed time step. For a FEM-DEM model, the critical time step (Δt) is determined based on Eqs. (7)–(10) [12]. In this study, Δt is governed by Δt_{DEM}, which is 6.53×10^{-6} s.

Table 2 Scaled DEM input parameters

Parameter	Value
Specific gravity	2.20
Particle diameter (mm)	6–10
Coefficient of friction	0.306
Normal and shear stiffnesses (k_n and k_s) (N/m)	1.86×10^6
Normal and shear damping ratios (β_n and β_s)	0.1

$$\Delta t \leq min\left\{\Delta t_{DEM}, \Delta t_{FEM}\right\} \tag{7}$$

$$\Delta t_{DEM} = TSSFAC \bullet 0.2 \bullet \pi \bullet \sqrt{\frac{m}{k_n}} \tag{8}$$

$$\Delta t_{FEM} = \frac{l_{min}}{c} \tag{9}$$

$$c = \sqrt{\frac{E(1-\nu)}{(1+\nu)(1-2\nu)\rho}} \tag{10}$$

where Δt_{DEM} and Δt_{FEM} are the critical time steps for the discrete and finite elements, respectively; *TSSFAC* is a time step scale factor in LS-DYNA, and the default value of $TSSFAC = 0.9$ is used in this study; m and k_n are the mass and normal stiffness of the DEM particles, respectively; l_{min} is the minimum effective length of the finite elements; c is the velocity of the elastic wave; and E, ν and ρ are the Young's modulus, Poisson's ratio and the mass density of the finite elements, respectively.

Similar to the experimental tests, both the 3.64 and 5.46 kg scale modules were examined in the simulations to investigate the effect of the module's weight on ground improvement. In this study, the modules were operated at a speed of 299 mm/s, which correspond to a prototype speed of 14 km/h. All simulations were conducted on the University of Adelaide's high-performance computer (2 × Intel Xeon Gold 6248 Processor @ 2.4 GHz) with each taking approximately 25 days to complete.

3.2 Arrangement of measurement spheres

In the numerical simulation, porosities and stresses within a granular body can be quantified by means of measurement spheres. By placing measurement spheres in the region of interest, changes in porosities and stresses can be monitored

consistently within the sphere of interest. The size of the measurement spheres can affect the obtained porosity and stress results. Measurement spheres that are too small result in statistical errors and those that are too large result in a loss of resolution [17]. According to Chen et al. [18] and Li et al. [46], measurement spheres should incorporate at least 50 particles. In this study, the diameter of the measurement spheres was selected to be 50 mm, which includes more than 50 particles in each sphere. Measurement spheres were created to facilitate the examination of porosity changes with respect to RDC, as shown in Fig. 5. These measurement spheres are fixed at their respective locations throughout the simulation. In total, 60 measurement spheres (M1 to M60) were generated and porosity results were then used to assess the effectiveness of RDC. These measurement spheres were aggregated into 12 groups based on the horizontal distances from the left corner of the chamber and were numbered G1 to G12, as shown in Fig. 5. It is important to note that, as mentioned earlier and in order to minimise boundary effects, ground improvement is assessed only in the central section of the chamber, which concerns the region incorporating the G3, G4, G9 and G10 aggregated measurement spheres shown in Fig. 5.

4 Results and Discussion

4.1 Verification of the DEM model

The ability of the numerical model in predicting ground settlements with respect to the number of passes is examined against the experimental test results. Consistent with Chen et al. [8], in the numerical simulations, the front face of the chamber is divided into three regions and, only soil improvement that occur in the central region is used to assess the effectiveness of RDC, as this region is less

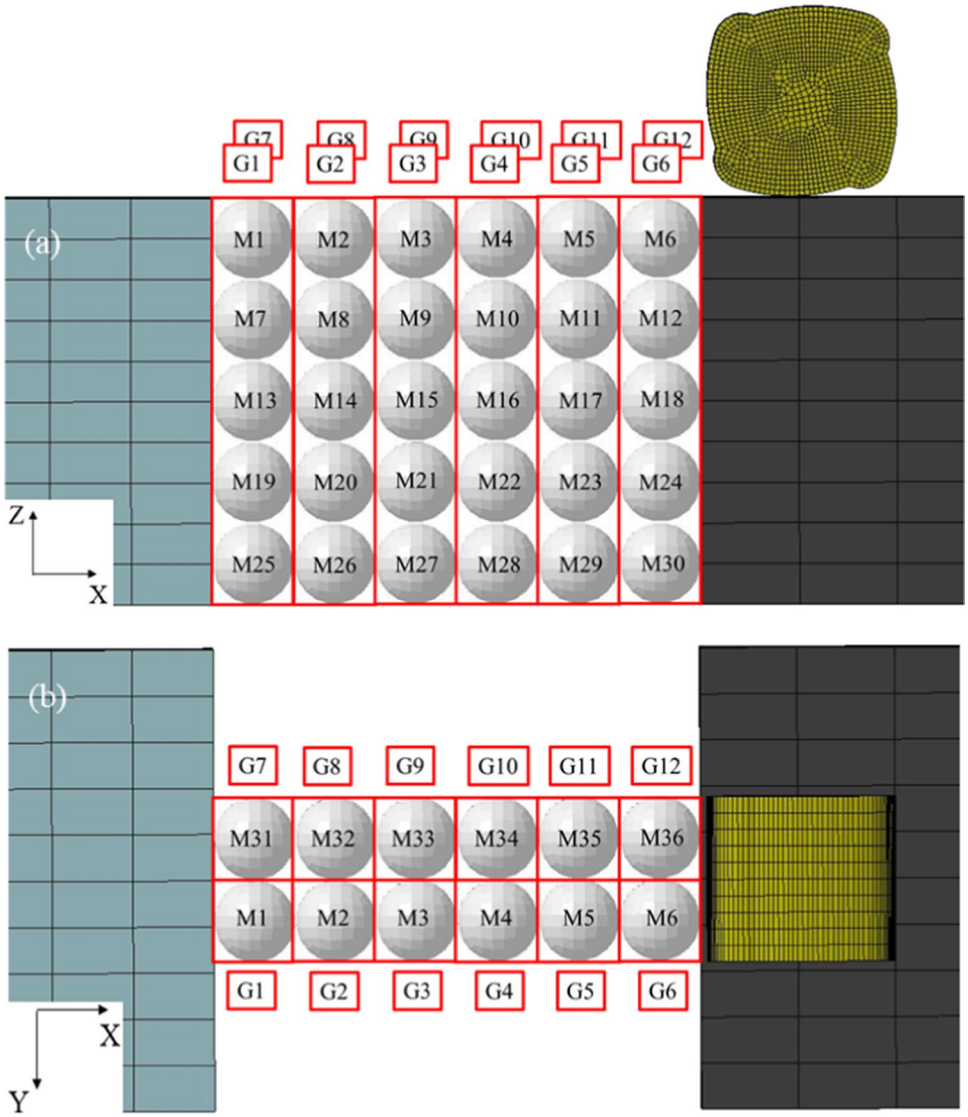

Fig. 5 Arrangement of the measurement spheres in the module traverse lane: **a** side view, **b** plan view

affected by the chamber's boundaries. Experimental ground settlements were obtained using a high-precision 3D surface scanner (EinScan Pro+) [8]. The module traverse lane was scanned after every 10 module passes and the displacement of each captured particle within the central region of the chamber was summed and then averaged to calculate the average ground settlement with respect to the number of passes. Consistent with Chen et al. [8], coordinates of an approximately one-particle thick layer of numerical particles, which is located at the ground surface of the module traverse lane, within the central region of the chamber, were recorded and averaged after every 10 module passes to obtain the numerical ground settlements. As shown in Fig. 6, the numerical model performs well. As indicated, the heavier module (5.46 kg module) produces larger ground settlements, as one would expect. In general, the ground settlements predicted by the numerical model are slightly different from those measured experimentally. There are a number of likely reasons for this. Firstly, the nature of the RDC physical scale model is more complex than the simplified numerical model, as the physical scale model involves, not only a 4-sided module, but also a spring-linkage system installed on both sides of the model (Fig. 4a), which is a feature of the full-scale module. This system stores some of the potential energy by compressing the springs when the model is towed forward. The springs subsequently release the stored energy at the time the module just begins to rotate about its corner and impact the ground. As a result, this spring-linkage system facilitates and augments the rotation of the module. Secondly, four wheels are incorporated in the physical scale model to assist in its smooth operation, in contrast to the prototype's two. Finally, the DEM model incorporates spherical particles, whereas the experimental tests involved angular fused quartz.

In addition, numerical average vertical displacements at different depths below the ground are compared with those obtained from the experiments to validate the behaviour of the numerical model. Experimental soil displacements below the ground were measured from the movement of a one-particle thick layer of dyed fused quartz located along the centreline of the module compacted area, using a CCD camera and the PIV system [8]. In the PIV analysis, subsets with a diameter of approximately 25 mm were adopted. The measured vertical displacements from the central region of the chamber were averaged over the subsets which had centres located at 50, 100, 150 and 200 mm depths below the ground. In order to compare the numerical results with those obtained experimentally, the numerical soil displacements were calculated by averaging coordinate changes of approximately a one-particle thick layer located along with the centreline of the roller traverse lane at 37.5–62.5, 87.5–112.5, 137.5–162.5 and 187.5–212.5 mm depths below the ground within the central region of the chamber. As shown in Fig. 7, the numerical soil displacements are in excellent agreement with experimental results, for both the 3.64 and 5.46 kg scale modules after 40 passes. Displacements at depth of zero in Fig. 7 represent the ground settlements obtained after 40 passes in Fig. 6. A summary of the detailed soil displacements for the 3.64 kg module travelling at 299 mm/s is given in Table 3. It can be seen that maximum difference between

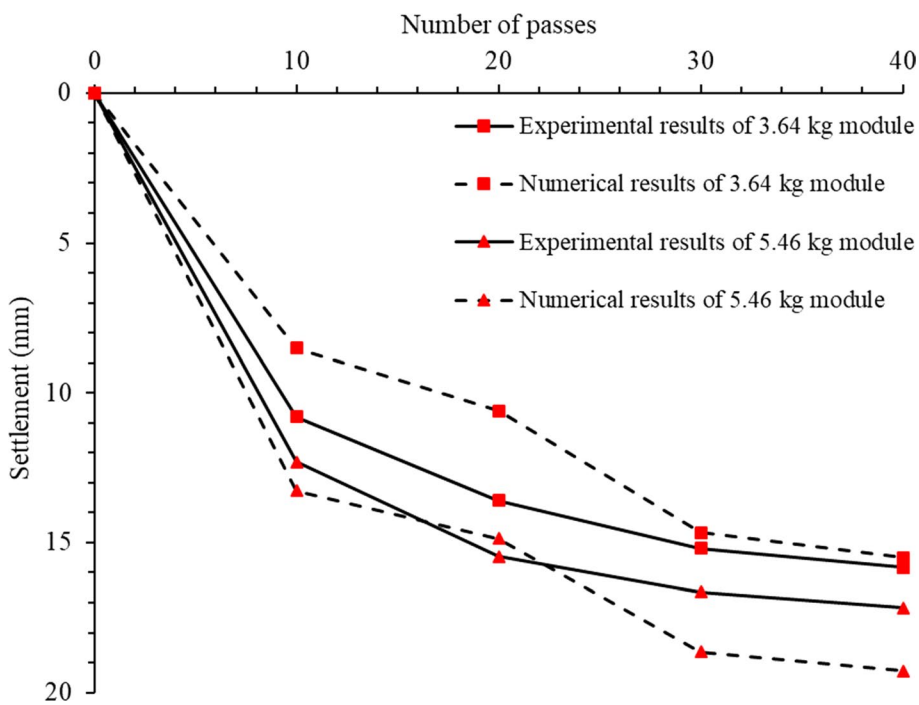

Fig. 6 Ground settlements obtained from both the 3.64 and 5.46 kg modules

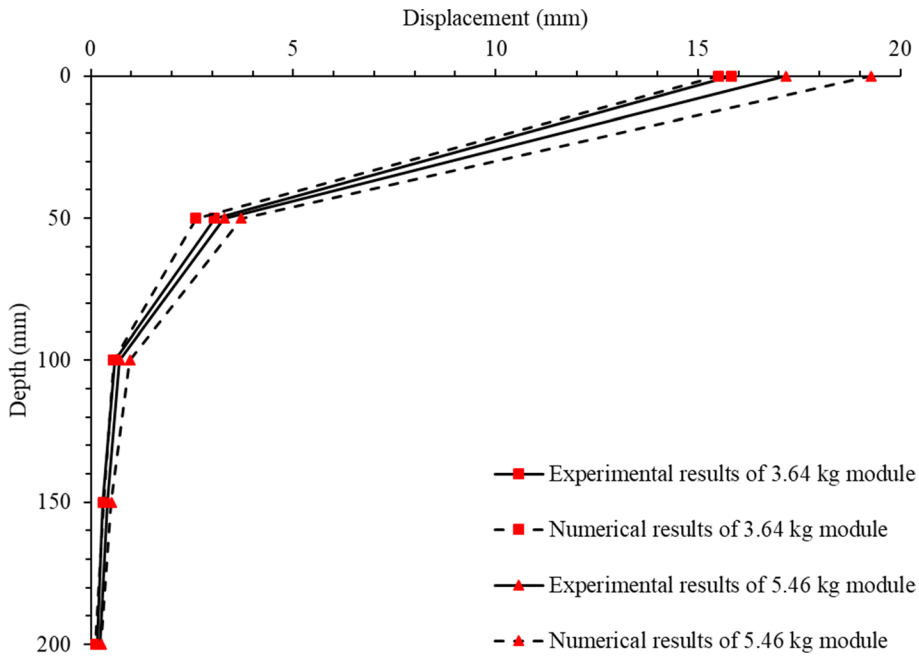

Fig. 7 Soil displacements after 40 passes for both the 3.64 and 5.46 kg modules

Table 3 Detailed soil displacement results for 3.64 kg module traverses at a speed of 299 mm/s after 40 passes

Depth (mm)	Displacement (mm)		
	Experimental	Numerical	Difference (%)
0	15.83	15.51	–0.32 (–2%)
50	3.06	2.59	–0.46 (–15.1%)
100	0.59	0.56	–0.03 (–5.9%)
150	0.29	0.32	0.03 (8.8%)
200	0.15	0.11	–0.04 (–25.5%)

the numerical and experimental results is 0.46 mm, and in terms of percentage difference, 25.5%. It should be noted that the 25.5% relates to a difference of 0.04 mm. It is clear that these differences are modest and, as a result, it can be concluded that the numerical model reasonably predicts the soil displacements observed in the experimental model tests.

4.2 Porosity changes relative to the roller's motion

Figure 8 shows the motion of the module, the location of the measurement spheres and the velocity vectors of soil particles at different times during the first pass of the 5.46 kg module operating at 299 mm/s. Time, $t = 0$ s is defined as the moment when the module just leaves the timber frame at the right edge of the chamber (Fig. 8a). The module then compacts the soil between $t = 0.2$ to 1.0 s (Figs. 8b, c, d, e and f). When $t = 1.2$ s, the module leaves the chamber and travels to the left timber frame (Fig. 8g). In general, it can be seen from the velocity vectors in Figs. 8c and d that, when the module compacts the ground, the predominant motion of the particles is in a forward (to the left) and downward direction. In addition, it can be seen from Figs. 8b, e and f that the particle displacements near the edges of the chamber are constrained, and therefore soil improvement is compromised, as one might expect.

In order to investigate the relationship between soil movements, porosities and the motion of the roller, the porosities measured by measurement spheres (M1 to M12), with respect to the time and motion of the 5.46 kg module travelling at 299 mm/s in Fig. 8, are presented in Fig. 9 for the first pass. The porosities are presented within each of the measurement spheres, and in parentheses, the incremental changes in porosity from the previous time step are also included. It is worth noting that the average particle diameter is 8 mm and each measurement sphere contains approximately 110 particles, which means that the porosity obtained from each measurement sphere is based on 0.27% of the total number of particles. As a result, there will inevitably be some fluctuations due to the necessary but limited size of the measurement spheres. At $t = 0.2$ s (Fig. 9b), the module impacts the soil located to the right of measurement sphere M6. It can be observed from the velocity vectors that the soil located to the right of M6 moves to the left and downwards (Fig. 8b), which results in the number of soil particles within M6 and M12 to increase, and, as a consequence, the porosities to decrease. As the module strikes the soil between M4 and M5 at $t = 0.4$ s (Fig. 9c), the soil behind the module displaces upwards and to the right (Fig. 8c), which results in the number of particles within M5 increases, and hence the porosity decreases. The porosities of M3 and M4 increase significantly since the soil located at M3

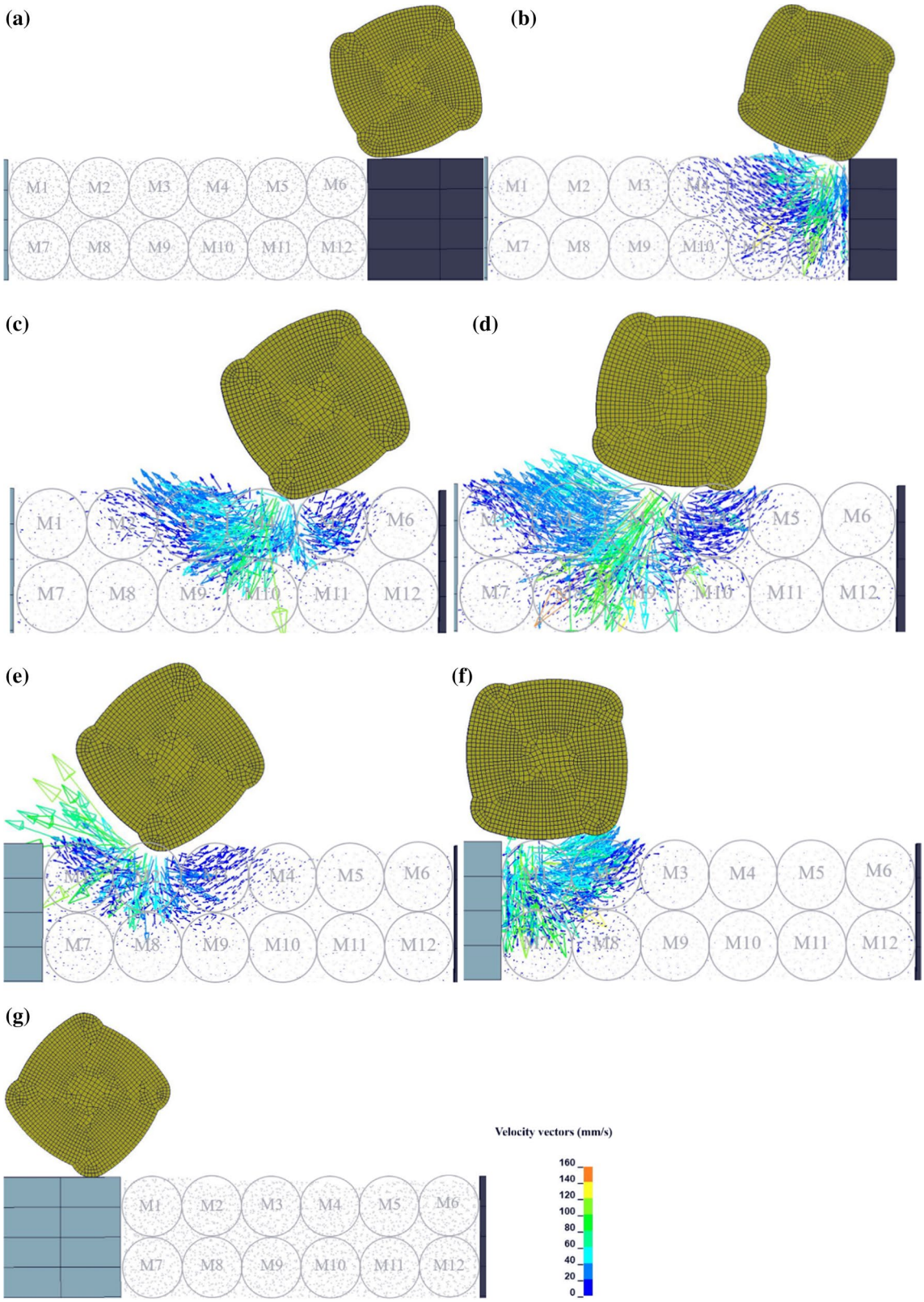

Fig. 8 Velocity vectors of the soil relative to the motion of the 5.46 kg module at different times: **a** t = 0 s, **b** t = 0.2 s, **c** t = 0.4 s, **d** t = 0.6 s, **e** t = 0.8 s, **f** t = 1.0 s, **g** t = 1.2 s

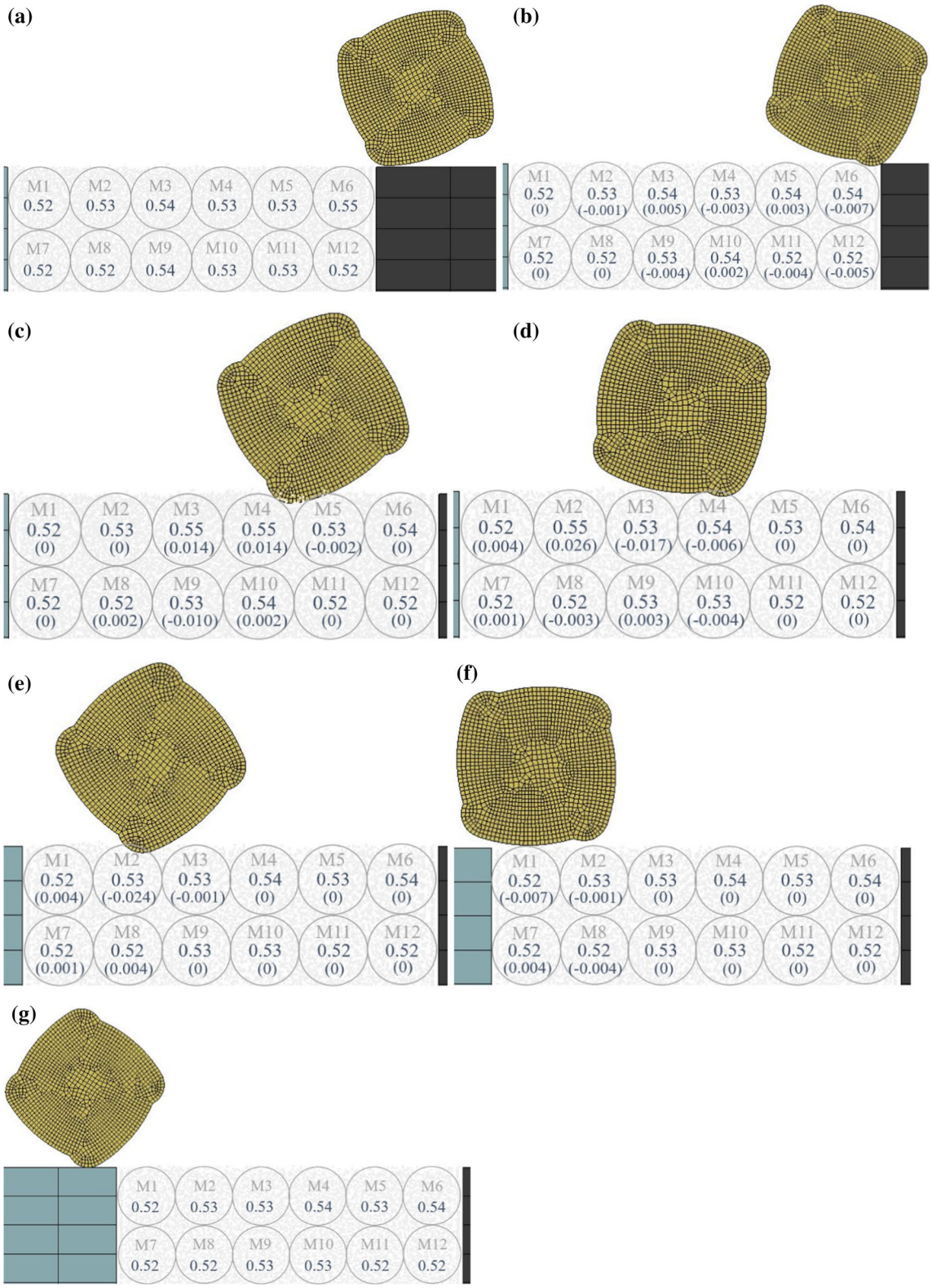

Fig. 9 Soil porosities relative to the motion of the 5.46 kg module at different times: **a** t = 0 s, **b** t = 0.2 s, **c** t = 0.4 s, **d** t = 0.6 s, **e** t = 0.8 s, **f** t = 1.0 s, **g** t = 1.2 s. The incremental change in porosity from the previous time step is given in parentheses

and M4 moves to the left. The particles located near M10 are pushed towards M9, therefore, the porosities within M10 and M9 increase and decrease, respectively. When the module impacts the soil located between M3 and M4 ($t = 0.6$ s, Fig. 9d), the soil near M3 and M4 is compacted and the porosities of M3 and M4 reduce to 0.53 and 0.54, respectively. The porosities of M1 and M2 increase since the soil located at these areas displaces upwards. Because the module travels away from the areas of M5, M6, M11 and M12, the porosities within these spheres remain constant. Again, the porosity of M1 shows an increasing trend since the soil located in this area moves upwards when the module strikes the soil at M2 ($t = 0.8$ s, Fig. 9e). The soil near M2 displaces downwards at $t = 0.8$ s, which results in the porosity at M2 to decrease. When $t = 1.0$ s (Fig. 9f), the soil near M1 is compacted and settles, therefore, the porosity of M1 decreases. A small portion of the soil located near M7 displaces to M8, which results in the porosities of M7 and M8 to increase and diminish, respectively. Finally, Fig. 9g shows the porosities after the first pass of the 5.46 kg module.

To understand better soil porosity change with respect to the motion of the module, soil porosities recorded by various measurement spheres are plotted against time. Figure 10 presents the variation of porosities with respect to the time and motion of the 5.46 kg module travelling at 299 mm/s in Figs. 8 and 9. The origin of the horizontal axis (time) in Fig. 10 is set at the right-hand-side of the plot to maintain consistency with the module's direction of travel. In general, it can be seen clearly that the measured porosities change significantly with the motion of the roller. When the porosities measured by M1–M6 are compared with those recorded by M7–M12, a greater variation of porosities is observed with the former since the compactive energy imparted by the module dissipates with depth, and hence, soil located at deeper depths is less influenced by the roller. The increase of porosities, such as those measured by M3 and M4 at 0.2–0.4 s, M2 at 0.4–0.6 s and M1 at 0.4–0.8 s, is due mainly to the soil being pushed and displaced along with the motion of the roller. The reduction in porosity is due to the soil located within these areas being compacted by the module. The porosities at $t = 1.2$ s show that after the first pass of the 5.46 kg module, the porosities at M2 and M6 decrease slightly and the porosities at M1, M3, M4 and M5 increase, since most of the soil particles located at the ground surface are compacted and displace downwards. In addition, the porosities measured by M8–M12 decrease significantly, which also indicate that the soil displaces downwards. As indicated by the velocity vectors and porosity changes, the compaction effects are limited to the soil located at relatively shallow depths, which is consistent with that reported by Chen et al. [8].

4.3 Optimum number of passes

In their laboratory study, Chen et al. [8] determined the optimum number of passes by assessing the averaged vertical incremental displacements caused by the module. In this paper, however, the optimum number of passes is examined using the changes in porosity of the soil located within the central region of the chamber beneath the module with respect to the number of passes. Variations of porosity with respect to the number of passes of the 3.64 and 5.46 kg modules are shown in Fig. 11. Additional measurement spheres were placed within the module compaction region to obtain higher resolutions of the porosity results. In general, the porosity decreases with increasing numbers of passes below 50 mm depth and the porosity increases with the number of passes above 50 mm depth. It can be seen that, for both the 3.64 and 5.46 kg modules, the most significant porosity changes occur within the first 30 passes, beyond which, the porosity change is modest. It can be observed from Fig. 11 that, the maximum porosity changes occur above 150 mm depth. In Fig. 12, the average porosities recorded by the measurement spheres located at 50–100 (M9, M10, M39 and M40) and 100–150 (M15, M16, M45 and M46) mm depths are plotted against the number of passes. The average porosity in the depth range of 0–50 mm is not included in Fig. 12. This is because the top surface undergoes disturbance by the roller module and as expected, the porosity between 0 and 50 mm increases throughout the 40 passes. It was suggested by Scott et al. [5] that, subsequent to RDC, the ground surface is always compacted by a conventional circular roller due to this disturbance and the undulating surface left by the impact roller. It can be seen from Fig. 12 that, as expected, the porosity at greater depths (100–150 mm) are less affected by the module, given that the compactive energy dissipates with depth. In general, there is no significant porosity change after 35 passes between 50 and 100 mm depth and no obvious porosity change after 30 passes below 100 mm depth, for the 3.64 kg module travelling at speed of 299 mm/s. Therefore, the optimum number of passes is around 35 passes for the 3.64 kg module and the soil characteristics examined. For the 5.46 kg module, porosity changes exhibit similar trends to those caused by the 3.64 kg module. Porosity between 50 and 100 mm exhibits no significant change after 35 passes and porosity below 100 mm shows no obvious change after approximately 30 passes. As a consequence, it can be concluded that, for the 5.46 kg module, the optimum number of passes is also around 35 passes for the soil located below 50 mm depth, for the soil type examined.

4.4 Effect of module weight

In this study, the effect of the module's weight on ground improvement is examined by quantifying the porosity

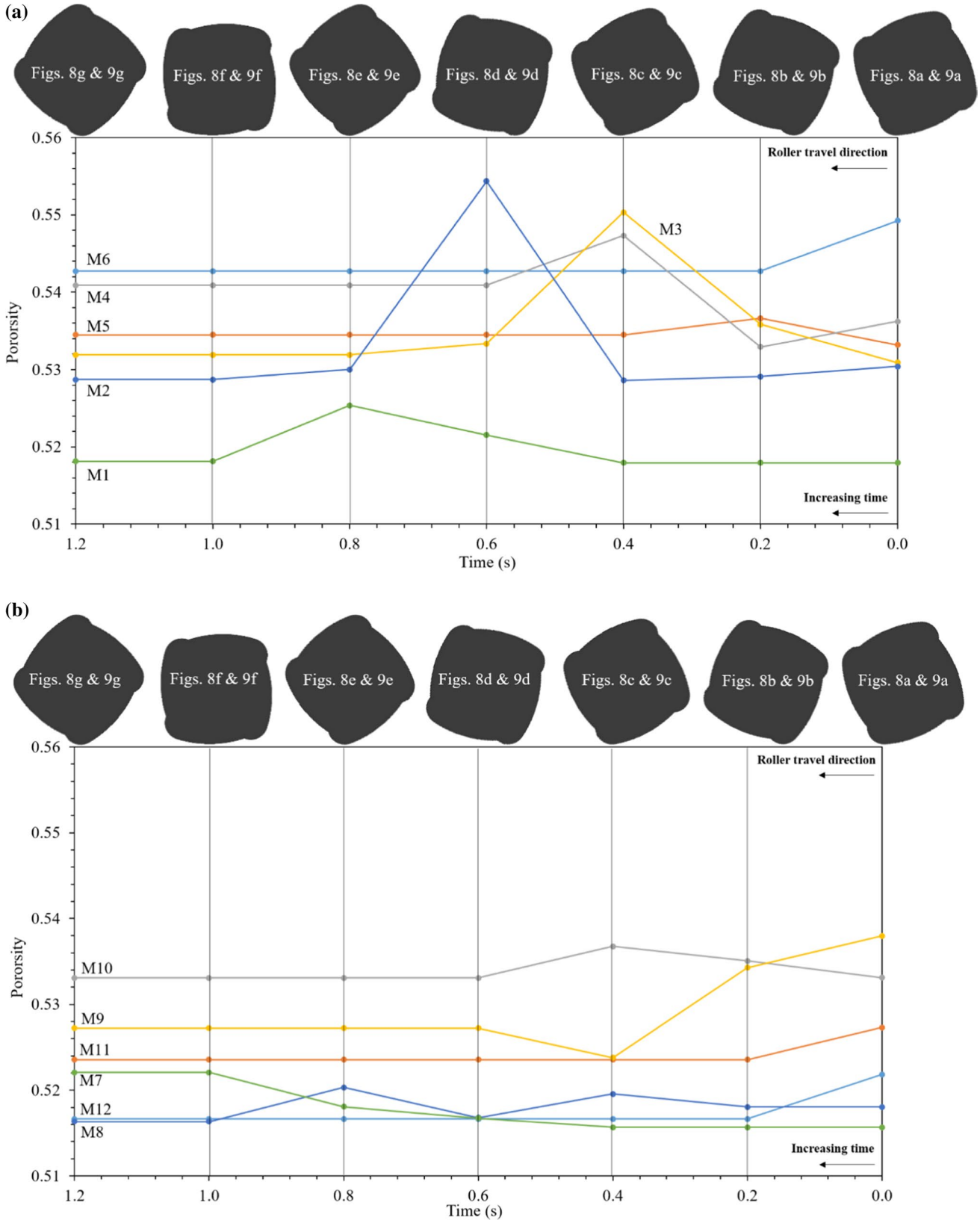

Fig. 10 Porosities measured by measurement spheres located at: **a** 25 mm depth below the ground, **b** 75 mm depth below the ground

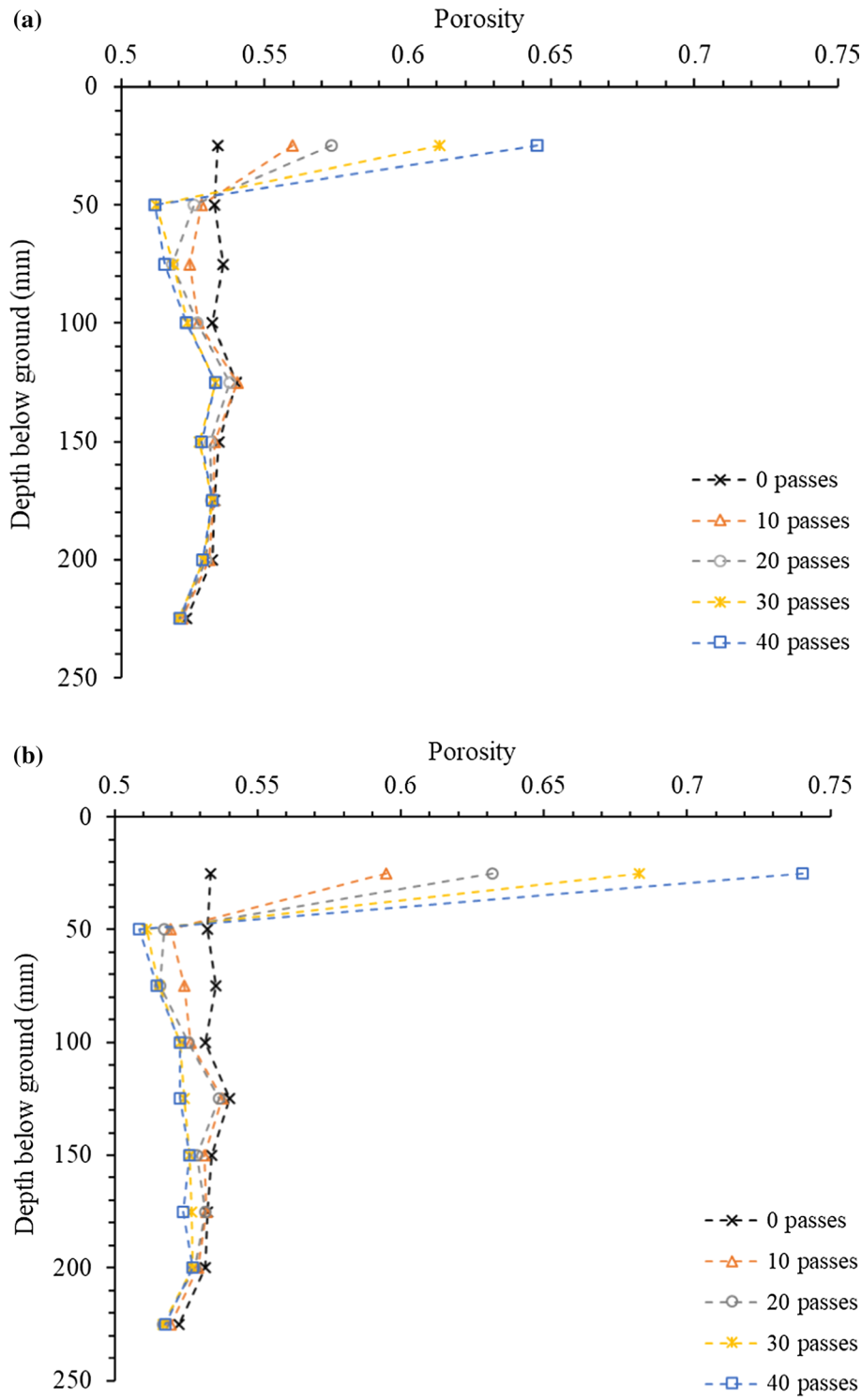

Fig. 11 Porosity changes with number of passes for: **a** 3.64 kg module, **b** 5.46 kg module

changes after 40 module passes. Table 4 presents the average porosity changes recorded by the measurement spheres located at G3, G4, G9 and G10 after 40 passes of both the 3.64 and 5.46 kg modules, respectively. It is noted that the leftmost column in Table 4 represents the locations of the centre points of the measurement spheres. For example, the depth of 75 mm refers to the centre point of the measurement spheres being 75 mm beneath the ground surface and, these spheres measure the soil porosity between 50 and 100 mm below the ground. In general, the 5.46 kg module results in greater porosity changes when compared with 3.64 kg module. Porosities increase near the ground surface and

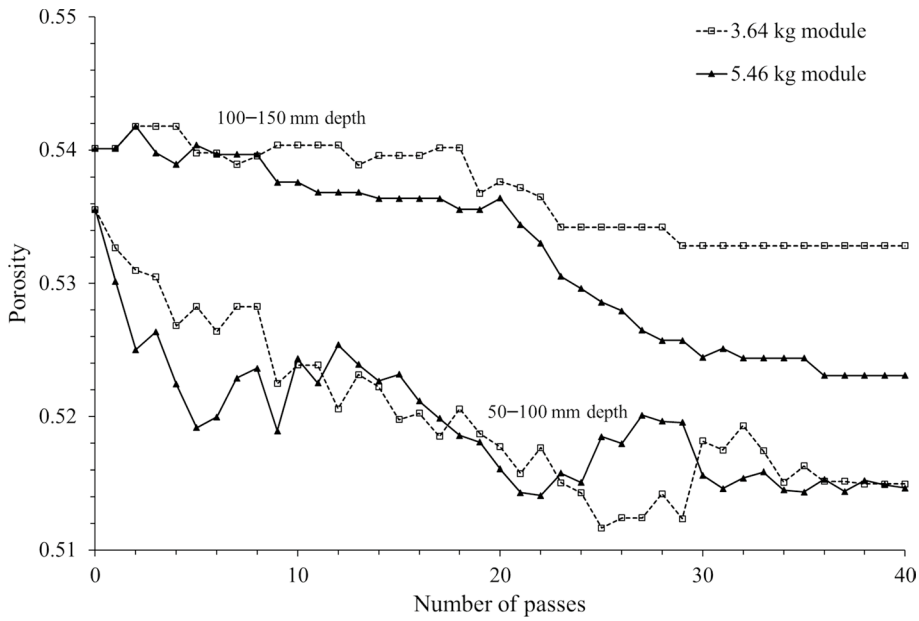

Fig. 12 Porosity changes at 50–100 and 100–150 mm depths for 3.64 and 5.46 kg modules

Table 4 The percentage porosity changes after 40 passes of the 3.64 and 5.46 kg modules, respectively

Depth (mm)	3.64 kg module (%)	5.46 kg module (%)
25	20.91	38.71
75	–3.84	–3.90
125	–1.35	–3.15
175	–0.18	–1.62
225	–0.42	–0.95

decrease within the soil at greater depth. As is normal with RDC, the soil near the ground surface decreases in density (i.e. increases in porosity) as a result of the characteristics of the motion of the module [5]. The maximum porosity reduction of the soil occurs at a depth between 50 and 100 mm. At greater depths (e.g. 150–200 mm), the porosity decreases less markedly. The porosity is almost unchanged at the base of the chamber during the test, which indicates that the soil at the base is less affected by the module, as one would expect. This conclusion is consistent with that obtained using the PIV technique as reported by Chen et al. [8]. The results presented in Table 4 show that the 5.46 kg (i.e. 12-tonne prototype) module increases the soil density to a greater extent than the 3.64 kg (i.e. 8-tonne prototype) module.

In order to compare the efficiency of the 3.64 and 5.46 kg modules further, the relative densities of the soil, with respect to the number of passes, are plotted for both modules travelling at a speed of 299 mm/s. Rather than porosity, changes in relative density of the soil, before and after compaction, are generally adopted in geotechnical engineering as an effective indicator of the effectiveness of compaction, since relative density is a measure of soil compactness. According to Salot et al. [47], in the numerical model, the maximum void ratio is obtained by pluviating particles under gravity. The minimum void ratio is obtained by pluviating particles in successive layers from the same approximate height of 350 mm, and a rigid plate is used to compact each layer to facilitate the densest arrangement of particles. The maximum and minimum void ratios of the numerical assembly are 0.853 and 0.632, respectively. Therefore, the relative densities of the soil between 100–150 mm depth are calculated based on the porosity changes, and are plotted in Fig. 13. This depth range is selected as it provides the greatest difference between these two modules. It can be observed that the post-compaction relative densities are greater than the pre-compaction relative densities for both the 3.64 and 5.46 kg modules, as one would expect. The 5.46 kg module results in greater soil density after the first 8 passes and the maximum relative densities are 72.9 and 60% for the 3.64 and 5.46 kg modules, respectively. As evidenced from the figure, fewer numbers of passes are needed when the heavier module is used. As a result, due to its heavier weight, the 5.46 kg module is more effective, and hence more efficient, than the 3.64 kg module.

As described by Duncan and Seed [48], soil compaction is treated as a loading and unloading process, which results in a significant increase of horizontal stress within the soil. The increase in horizontal stress after compaction is important for geotechnical design since it can be directly related to an increase in soil stiffness [49]. In addition, according to Massarsch and Fellenius [49], ground settlement is often adopted as the criterion for the specification of soil compaction projects and the input parameters for analytical methods,

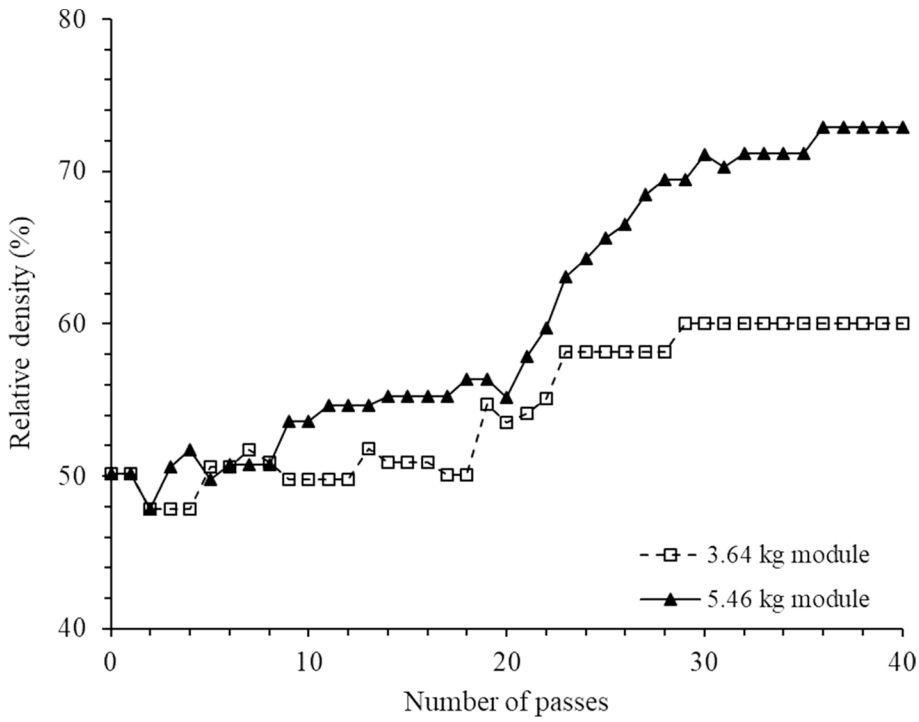

Fig. 13 Relative densities of soil at 100–150 mm depth with respect to number of passes for 3.64 and 5.46 kg modules operated at a speed of 299 mm/s

such as compression modulus and preconsolidation stress, which are used to predict ground settlement after compaction. However, the increase in soil preconsolidation stress is often neglected by the designer and this can often result in excessive compaction requirements and overestimated costs. As a result, the horizontal stresses recorded by the groups of measurement spheres located at G3, G4, G9 and G10 induced by the 3.64 and 5.46 kg modules are presented in Fig. 14. As can be seen, the horizontal stress increases significantly with the compaction of both the 3.64 and 5.46 kg modules. The heavier module induces a greater horizontal stress, as one would expect. When the horizontal stresses after 40 passes are compared with those recorded after 20 passes, it can be seen that the rate of increase of horizontal stress diminishes with respect to the number of passes for both module weights. This is consistent with that reported by Duncan and Seed [48]. They stated that the additional compactive energy applied to the compacted soil results in a much smaller increase in soil stress compared when against that applied to the uncompacted material.

5 Summary and conclusions

This paper has presented a series of three-dimensional finite element method (FEM)-discrete element method (DEM) simulations to analyse the behaviour of granular materials subjected to rolling dynamic compaction (RDC) due to a 4-sided impact roller. The FEM was used to simulate the roller module, the chamber and timber frames. The soil particles, on the other hand, were simulated using the DEM. The performance of the numerical model was validated against 1:13 scale, experimental tests based on displacements of the soil particles. The results showed that the numerical model can reasonably predict soil displacements at different depths below the ground. The behaviour of granular particles impacted by the scale module can be reproduced using the FEM and the DEM. The motion of the module and the porosities were plotted at different time intervals to help understand the soil porosity and density changes with respect to the motion of the module. Based on porosity changes obtained from measurement spheres, the effectiveness of two 1:13 scale models, weighing 3.64 and 5.46 kg, which represent the 8- and 12-tonne prototypes, was examined at an operating speed of 299 mm/s, corresponding to a prototype speed of 14 km/h. The heavier module produces greater ground improvement. The most significant porosity changes occur within the first 35 passes for both the 3.64 and 5.46 kg modules. The changes of porosity decrease with depth, and beyond around 200 mm depth below the ground surface, the porosity changes are negligible. Overall, the results of this study help to understand better the behaviour of the module on granular soils. However, inferences obtained in this study are based on the results of a single soil type. Future work needs to be implemented to assess the effectiveness of the scaled module in a variety of soil types and ground conditions.

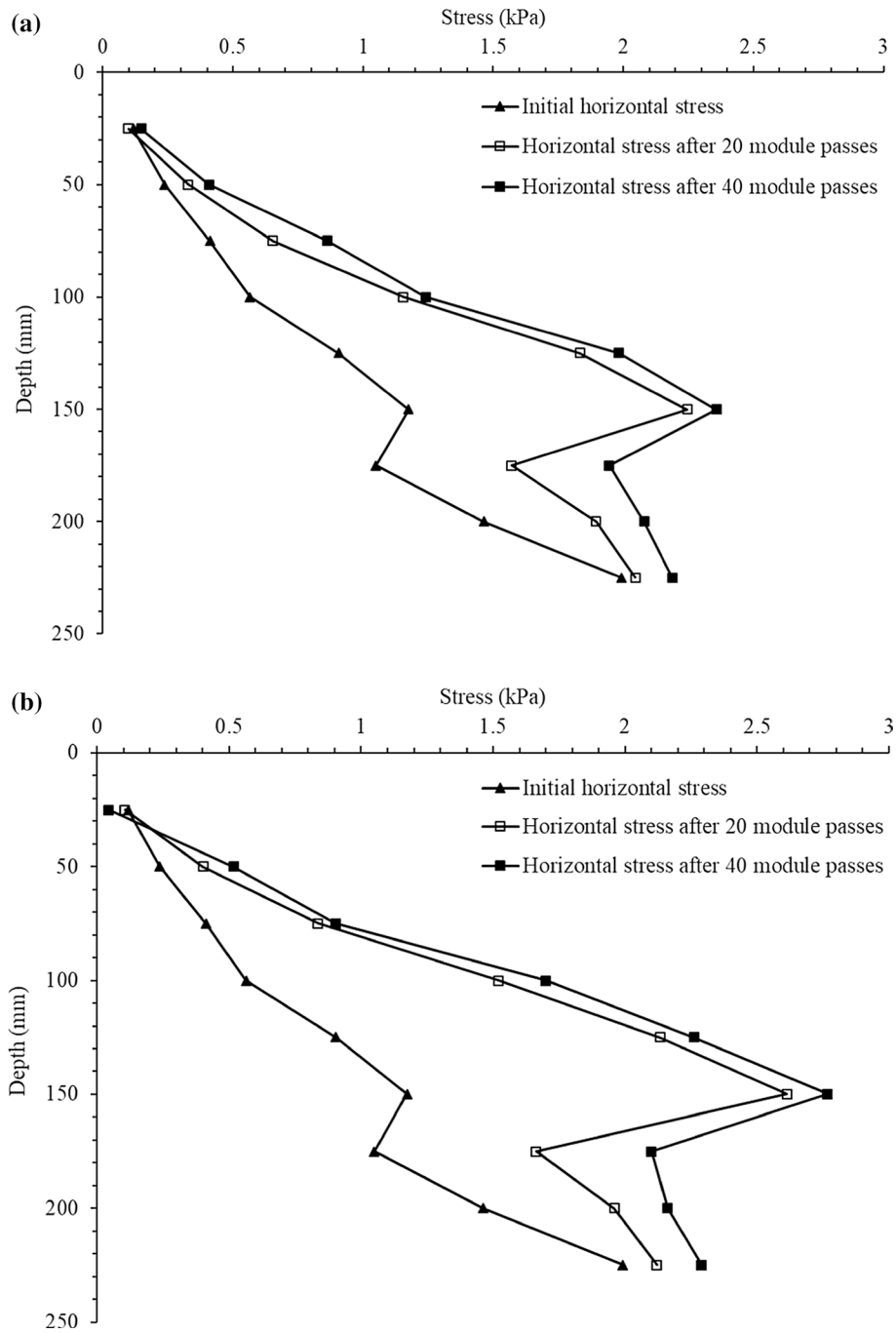

Fig. 14 Soil horizontal stress distribution for: **a** 3.64 kg module, **b** 5.46 kg module

Acknowledgements The authors wish to acknowledge the computational resources provided by the Phoenix HPC service at the University of Adelaide.

Funding This study was funded by Adelaide Graduate Research Scholarship.

Declarations

Conflict of interest The authors declare that they have no conflict of interest.

References

1. Avalle, D., Carter, J.: Evaluating the improvement from impact rolling on sand. In: Proceedings of the 6th International Conference on Ground Improvement Techniques, Coimbra, Portugal. p. 8. (2005)
2. Pinard, M.: Innovative developments in compaction technology using high energy impact compactors. In: Proceedings 8th Australia New Zealand Conference on Geomechanics: Consolidating Knowledge, Australian Geomechanics Society. p. 775. (1999)
3. Jaksa, M.B., Scott, B.T., Mentha, N., Symons, A., Pointon, S., Wrightson, P., Syamsuddin, E.: Quantifying the zone of

influence of the impact roller. In: ISSMGE-TC 211 International Symposium on Ground Improvement IS-GI Brussels. 41–52. (2012)
4. Scott, B., Jaksa, M.: Evaluating rolling dynamic compaction of fill using CPT. In: Proceedings of the 3rd International Symposium on Cone Penetration Testing. pp. 941–948. (2014)
5. Scott, B., Jaksa, M., Syamsuddin, E.: Verification of an impact rolling compaction trial using various in situ testing methods. In: Proceedings of the 5th International Conference on Geotechnical and Geophysical Site Characterisation (2016)
6. Rajarathnam, P., Masoudian, M.S., Airey, D.W., Jaksa, M.B.: Model tests of rolling dynamic compaction. In: Proceedings of the 19th Southeast Asian Geotechnical Conf. and 2nd AGSSEA Conf. Kuala Lumpur Malaysia. pp. 505–510. (2016)
7. Chung, O., Scott, B., Jaksa, M., Kuo, Y., Airey, D.: Physical modeling of rolling dynamic compaction. In: Proceedings of the 19th International Conference on Soil Mechanics and Geotechnical Engineering, Seoul, Korea, Sept. 18–22, pp. 905–908. (2017)
8. Chen, Y., Jaksa, M., Kuo, Y., Airey, D.: Experimental Analysis of Rolling Dynamic Compaction Using Transparent Soils and Particle Image Velocimetry. Canadian Geotechnical Journal. (2021) Available from https://doi.org/10.1139/cgj-2020-0573.
9. Altaee, A., Fellenius, B.H.: Physical modeling in sand. Can. Geotech. J. **31**(3), 420–431 (1994)
10. Kuo, Y., Jaksa, M., Scott, B., Bradley, A., Power, C., Crisp, A., Jiang, J.: Assessing the effectiveness of rolling dynamic compaction. In: Proceedings of the 18th International Conference on Soil Mechanics and Geotechnical Engineering, Paris. 1930–1312 (2013)
11. Bradley, A.C., Jaksa, M.B., Kuo, Y.-L.: Examining the kinematics and energy of the four-sided impact roller. Proc. Inst. Civil Eng. Ground Improvement **172**(4), 297–304 (2019). https://doi.org/10.1680/jgrim.18.00124
12. LSTC: LS-DYNA KEYWORD USER'S MANUAL. Livermore, California: Livermore Software Technology Corporation, ISBN: 0–9778540–2–7. (2018)
13. Cundall, P.A., Strack, O.D.: A discrete numerical model for granular assemblies. Geotechnique **29**(1), 47–65 (1979)
14. Gabrieli, F., Cola, S., Calvetti, F.: Use of an up-scaled DEM model for analysing the behaviour of a shallow foundation on a model slope. Geomech. Geoeng. Int. J. **4**(2), 109–122 (2009)
15. Farsi, A., Xiang, J., Latham, J., Pullen, A., Carlsson, M., Stitt, E., Marigo, M.: An application of the finite-discrete element method in the simulation of ceramic breakage: methodology for a validation study for alumina specimens (2015)
16. Forsström, D., Jonsén, P.: Calibration and validation of a large scale abrasive wear model by coupling DEM-FEM: Local failure prediction from abrasive wear of tipper bodies during unloading of granular material. Eng. Fail. Anal. **66**, 274–283 (2016)
17. Jiang, M., Dai, Y., Cui, L., Shen, Z., Wang, X.: Investigating mechanism of inclined CPT in granular ground using DEM. Granular Matter **16**(5), 785–796 (2014)
18. Chen, Y., Deng, A., Wang, A., Sun, H.: Performance of screw–shaft pile in sand: Model test and DEM simulation. Comput. Geotech. **104**, 118–130 (2018)
19. Huang, M., Chen, Y., Gu, X.: Discrete element modeling of soil-structure interface behavior under cyclic loading. Comput. Geotech. **107**, 14–24 (2019)
20. Coetzee, C.J.: Review: Calibration of the discrete element method. Powder Technol. **310**, 104–142 (2017). https://doi.org/10.1016/j.powtec.2017.01.015
21. Calvetti, F., Viggiani, G., Tamagnini, C.: A numerical investigation of the incremental behavior of granular soils. Rivista italiana di geotecnica **37**(3), 11–29 (2003)
22. Calvetti, F., Di Prisco, C., Nova, R.: Experimental and numerical analysis of soil–pipe interaction. J. Geotech. Geoenviron. Eng. **130**(12), 1292–1299 (2004)
23. Wang, Y.-H., Leung, S.-C.: A particulate-scale investigation of cemented sand behavior. Can. Geotech. J. **45**(1), 29–44 (2008)
24. Antypov, D., Elliott, J.: On an analytical solution for the damped Hertzian spring. EPL (Europhys. Lett.) **94**(5), 50004 (2011)
25. Imre, B., Räbsamen, S., Springman, S.M.: A coefficient of restitution of rock materials. Comput. Geosci. **34**(4), 339–350 (2008)
26. Chou, H., Lee, C., Chung, Y., Hsiau, S.: Discrete element modelling and experimental validation for the falling process of dry granular steps. Powder Technol. **231**, 122–134 (2012)
27. González-Montellano, C., Fuentes, J., Ayuga-Téllez, E., Ayuga, F.: Determination of the mechanical properties of maize grains and olives required for use in DEM simulations. J. Food Eng. **111**(4), 553–562 (2012)
28. Mahabadi, O., Lisjak, A., Grasselli, G., Lukas, T., Munjiza, A.: Numerical modelling of a triaxial test of homogeneous rocks using the combined finite-discrete element method. In: Proc. European Rock Mechanics Symp.(EUROCK2010), Lausanne, Switzerland, pp. 173–176 (2010)
29. Kozicki, J., Tejchman, J., Mühlhaus, H.B.: Discrete simulations of a triaxial compression test for sand by DEM. Int. J. Numer. Anal. Meth. Geomech. **38**(18), 1923–1952 (2014)
30. Gu, M., Han, J., Zhao, M.: Three-dimensional discrete-element method analysis of stresses and deformations of a single geogrid-encased stone column. Int. J. Geomech. **17**(9), 04017070 (2017)
31. Da Cruz, F., Emam, S., Prochnow, M., Roux, J.-N., Chevoir, F.: Rheophysics of dense granular materials: Discrete simulation of plane shear flows. Phys. Rev. E **72**(2), 021309 (2005)
32. Xu, W., Zeng, H., Yang, P., Zang, M.: Numerical analysis on tractive performance of off-road tire on gravel road using a calibrated finite element method–discrete element method model and experimental validation. Proc. Inst. Mech. Eng. Part D J. Automobile Eng. **234**(14), 3440–3457 (2020)
33. Zhang, A., Jiang, M., Thornton, C.: A coupled CFD-DEM method with moving mesh for simulating undrained triaxial tests on granular soils. Granular Matter **22**(1), 1–13 (2020)
34. Wu, K., Sun, W., Liu, S., Zhang, X.: Study of shear behavior of granular materials by 3D DEM simulation of the triaxial test in the membrane boundary condition. Advanced Powder Technology (2021).
35. Sadek, M.A., Chen, Y.: Microproperties calibration of discrete element models for soil-tool interaction. In: 2014 Montreal, Quebec Canada July 13–July 16, American Society of Agricultural and Biological Engineers, p. 1. (2014)
36. Nandanwar, M.: Measurement and simulation of triaxial compression tests for a sandy loam soil. (2015).
37. Bian, X., Nan, C., Xiao, F., Zhou, Z., Wang, Z.: FEM analysis of impaction effect for non-column wheels of compacting roller. Chinese Journal of Mechanical Engineering **10** (2002).
38. Yang, B., Jiao, Y., Lei, S.: A study on the effects of microparameters on macroproperties for specimens created by bonded particles. Eng. Comput. **23**(6), 607–631 (2006)
39. Ciantia, M., Arroyo Alvarez de Toledo, M., Calvetti, F., Gens Solé, A.: An approach to enhance efficiency of DEM modelling of soils with crushable grains. Géotechnique **65**(2), 91–110 (2015).
40. Tatsuoka, F.: Particle size effects on bearing capacity of footing on granular material. Proc. IS-NAGOYA, (1997).
41. Evans, T.M., Valdes, J.R.: The microstructure of particulate mixtures in one-dimensional compression: numerical studies. Granular Matter **13**(5), 657–669 (2011)
42. Ciantia, M.O., Arroyo, M., Butlanska, J., Gens, A.: DEM modelling of cone penetration tests in a double-porosity crushable granular material. Comput. Geotech. **73**, 109–127 (2016)

43. Zhou, W., Ma, X., Ng, T.-T., Ma, G., Li, S.-L.: Numerical and experimental verification of a damping model used in DEM. Granular Matter **18**(1), 1 (2016)
44. Wang, C., Deng, A., Taheri, A.: Three-dimensional discrete element modeling of direct shear test for granular rubber–sand. Comput. Geotech. **97**, 204–216 (2018)
45. Feng, Y., Owen, D.: Discrete element modelling of large scale particle systems—I: exact scaling laws. Comput. Particle Mech. **1**(2), 159–168 (2014)
46. Li, L., Wu, W., El Naggar, M.H., Mei, G., Liang, R.: DEM analysis of the sand plug behavior during the installation process of open-ended pile. Comput. Geotech. **109**, 23–33 (2019)
47. Salot, C., Gotteland, P., Villard, P.: Influence of relative density on granular materials behavior: DEM simulations of triaxial tests. Granular Matter **11**(4), 221–236 (2009)
48. Duncan, J.M., Seed, R.B.: Compaction-induced earth pressures under K 0-conditions. J. Geotech. Eng. **112**(1), 1–22 (1986)
49. Massarsch, K., Fellenius, B.: Deep Compaction of Sand Causing Horizontal Stress Change.

Publisher's Note Springer Nature remains neutral with regard to jurisdictional claims in published maps and institutional affiliations.